# A Fourier Optics Tool to Derive the Plane Wave Spectrum of Quasi-Optical Systems [EM Programmer's Notebook]

Zhang, H.; Dabironezare, S. O.; Carluccio, G.; Neto, A.; Llombart, N.

**DOI**
10.1109/MAP.2020.3027233

**Publication date**
2021

**Document Version**
Accepted author manuscript

**Published in**
IEEE Antennas and Propagation Magazine

# A Fourier Optics Tool to Derive the Plane Wave Spectrum of Quasi-Optical Systems

Huasheng Zhang, Shahab Oddin Dabironezare, *Student Member*, *IEEE*, Giorgio Carluccio, *Member*, *IEEE*, Andrea Neto, *Fellow*, *IEEE*, Nuria Llombart, *Fellow*, *IEEE*

***Abstract*—We present a freely accessible graphical user interface for analysing antenna-fed Quasi-Optical systems in reception. This analysis is presented here for four widely used canonical Quasi-Optical components: parabolic reflectors, elliptical, extended hemispherical, and hyperbolic lenses. The employed methods are Geometrical Optics and Fourier Optics. Specifically, Quasi-Optical components are illuminated by incident plane waves. By using a Geometrical Optics based propagation code, the scattered fields are evaluated at an equivalent sphere centred on the primary focus of the component. The Fourier Optics methodology is then used to represent the scattered fields over the focal plane as Plane Wave Spectrum. A field correlation between this spectrum and the antenna feed radiating without the Quasi-Optical component is implemented to evaluate the induced open-circuit voltage on the feed in reception. By performing a field matching between these two spectral fields, feed designers can optimize the broadside and/or steering aperture efficiencies of Quasi-Optical systems in a fast manner. The tool is packaged into a MATLAB graphical user interface, which reports the efficiency terms, directivity and gain patterns of antenna-coupled Quasi-Optical systems. The described tool is validated via full-wave simulations with excellent agreement.**

***Index Terms*—Quasi-Optical systems, sub-millimetre wavelengths, antenna feeds, Geometrical Optics, Fourier Optics.**

## I. Introduction

In recent years, advanced Quasi-Optical (QO) based systems are emerging as the state-of-the-art solutions for sensing and imaging applications at (sub)-mm wavelengths: i.e. reflectors and dielectric lenses, are employed for astronomical observations [1]–[4], standoff personnel screening [5]–[9], and new generation of wireless communications [10]–[16]. To meet the demanding performance requirements in these systems, highly directive radiative beams are essential. In imaging scenarios, higher directivity leads to better angular resolution; in sensing and communication applications to a higher signal to noise ratio. To achieve these requirements, the QO components are typically used in combination with antenna feeds.

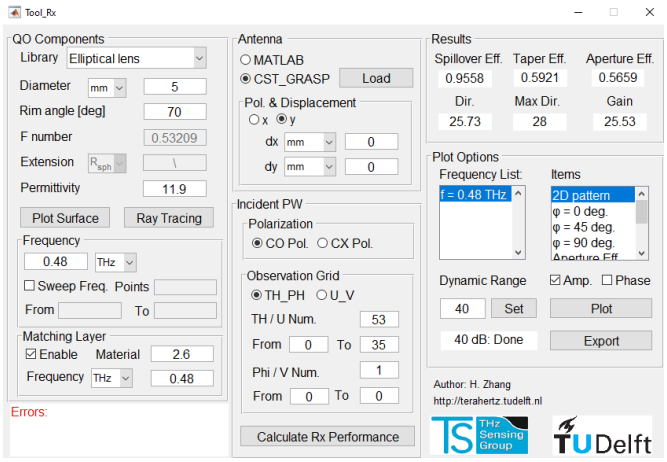


Fig. 1 User interface of the freely accessible MATLAB GUI.

Two of the widely used high-frequency techniques to analyse QO systems are ray tracing and Physical Optics (PO) which are packaged in commercial software such as OpticStudio [17], and GRASP [18], respectively. The ray tracing is an insightful method that can be used to evaluate the propagation of rays through a QO system providing first-order estimation of phase aberrations in the systems. However, this technique does not provide an accurate estimation of the co- and cross- polarized field distributions. On the other hand, PO technique is a well-established and accurate method to evaluate the fields radiated by electrically large scatterers. This method is suitable for optimizing the shape of reflectors coupled to standard feeds. However, in commercial software such as GRASP, the PO analysis of integrated lenses is not implemented.

Independently from the techniques adopted, QO components can be analysed either in transmission (Tx) or reception (Rx) modes. The reciprocity theorem states that the analyses in both modes are equivalent. However, to rapidly optimize the geometry of an antenna feed for a QO system, an analysis in Rx provides more insight with respect to the one in Tx. This is due to the fact that the field scattered by a QO component on its focal plane can be approximated quasi-analytically for a plane wave incidence using a Fourier Optics (FO) approach. Specifically, the incident field can be evaluated over an equivalent sphere centred at the focal plane of the QO

This work was supported by the European Research Council Starting Grant (ERC-2014-StG LAA-THz-CC), No. 639749.

H. Zhang, S. O. Dabironezare, G. Carluccio, A. Neto and N. Llombart are with the THz Sensing Group, Microelectronics Department, Delft University of Technology, 2628 CD Delft, The Netherlands (e-mail: h.zhang-12@tudelft.nl; dabironezare.shahab@ieee.org; g.carluccio@tudelft.nl; a.neto@tudelft.nl, n.llombartjuan@tudelft.nl).

The tool is freely accessible at http://terahertz.tudelft.nl.

component using a Geometrical Optics (GO) analysis [19], and the following propagation to the focal plane can be represented as Plane Wave Spectrum (PWS), [20] and [21].

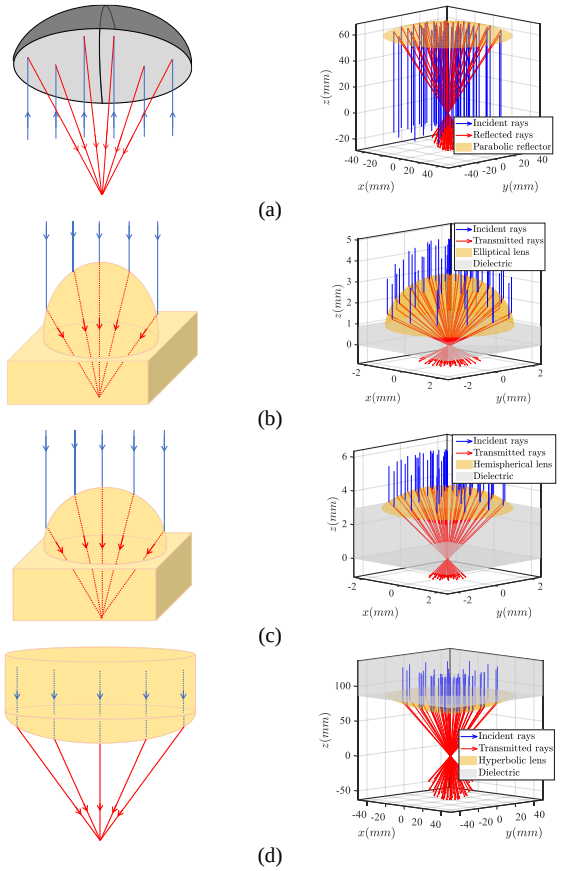


Fig. 2 The four considered geometries in the GUI with their corresponding ray tracing representations. Blue and red rays represent the incident plane waves and scattered rays propagating to the focal plane of the QO component, where the antenna feed is placed, respectively. Illustrations and the ray tracing representations obtained from the tool are shown in the left and right panels, respectively. (a) A parabolic reflector, (b) an elliptical lens, (c) an extended hemispherical lens, and (d) a hyperbolic lens.

By employing a field matching technique as in [16], [22], and [23], at the equivalent sphere, the geometry of the antenna feed can be optimized to match its radiated field to the incident PWS. Moreover, for multi-mode antennas coupled to incoherent detectors, the current distribution at the antenna aperture cannot be known independently from the incident field. Therefore, for multi-mode systems, the analysis in Rx as shown in [24], is in fact the only possibility to evaluate the optical efficiency. The incident PWS can also be linked to spectral techniques such as equivalent Floquet circuit model of absorbers or other periodic structures [25].

A numerical PO code can also be used to indirectly calculate the incident PWS of a QO component as the Fourier transform of the focal field as described in [26]. However, the GOFO method described here is a direct and much simpler approach (without the numerical Fourier transform integral) to obtain this PWS. In summary, FO approach is a powerful tool for synthesizing antennas coupled to QO components.

To our knowledge, currently no tool is available to implement the FO analysis in reception for a variety of QO components. The FO based analyses in the literature [20] and [21] are implemented mainly for parabolic reflectors and elliptical lenses for slightly off-broadside incident angles, which limits the design possibilities. Moreover, these codes are not implemented with a user interface. Consequently, a MATLAB based graphical user interface (GUI) is developed to analyse QO components in reception scenarios using the GOFO approach, as shown in Fig. 1. This tool is dedicated for analysing antenna-fed QO systems where a user can evaluate the aperture efficiency, at any angle, from a certain given antenna feed in a very fast manner. Four canonical QO components, parabolic reflectors, elliptical, extended hemispherical, and hyperbolic lenses, are implemented to provide multiple design possibilities, as shown in Fig. 2.

In the developed tool, a user-defined QO antenna system is modelled. The antenna system consists of a QO component and its geometrical parameters; the radiated fields of the antenna feed given as an input by the user; feed location at the focal plane of the QO component; and the observation grid of the reception pattern. The tool can generate ray tracing plots for all four QO components, as shown in Fig. 2. These plots provide a first-order understanding of the propagation scenarios, including the incident fields and the scattered GO fields. The incident PWS of QO components is then obtained using a GO based code similarly to [19], and is exportable ("Export" button in Fig. 1). This PWS can be used as an optimization goal for achieving field matching, and therefore maximizing the aperture efficiency for a certain angular direction. Moreover, the tool can evaluate directly the radiation performance of the entire user-defined QO antenna over a frequency band, similarly to [27]. Particularly, the power delivered to the load of the antenna feed, the aperture efficiency, the directivity, and gain patterns of the whole QO system are estimated. The results obtained by the tool are validated using the PO based code in GRASP [18] and full-wave simulations in CST MS [28].

## II. Plane Wave Spectrum of the Focal Fields

Let us consider an example scenario where a QO component is illuminated by an incident plane wave, as depicted in Fig. 3. This plane wave is expressed as $\vec{E}_i = E_0 \hat{p}_i e^{-j\vec{k}_i \cdot \vec{r}}$, where $E_0$ is the amplitude of the plane wave, $\hat{p}_i$ is the polarization, $\vec{k}_i = -k(\sin\theta_i \cos\phi_i \, \hat{x} + \sin\theta_i \sin\phi_i \, \hat{y} + \cos\theta_i \, \hat{z})$ is the wave-vector, $k$ is the propagation constant of the medium where the plane wave is present, $\theta_i$ and $\phi_i$ represent the elevation and azimuth incident angles, respectively.

The field scattered by the QO component on its focal plane is represented as an integral of the PWS. To realize this step, an equivalent sphere centred at the focal point of the QO component, referred to as the FO sphere, is introduced (see Fig. 3), where $R_{FO}$ is the radius of this sphere, and it is chosen as large as possible to enlarge the applicability region of the FO method; and $\theta_0$ is the maximum rim elevation angle of the QO component. The field scattered by the QO component is evaluated over this equivalent surface using a GO approach.

The field at the focal plane of the QO component can be calculated using the PO radiation integral via the introduction of equivalent surface currents which are proportional to the GO fields. By asymptotically evaluating the PO radiation integral for observation points close to the focus of the component, which leads to amplitude, vector and phase approximations of the integrand, one can represent the focal field as an inverse Fourier transform [20]:

$$\vec{e}_f(\vec{\rho},\vec{k}_i) = \frac{1}{4\pi^2}\iint_{-\infty}^{+\infty} \vec{E}_{FO}(k_x,k_y,\vec{k}_i)e^{j\vec{k}_\rho\cdot\vec{\rho}}dk_xdk_y \quad (1a)$$

$$\vec{h}_f(\vec{\rho},\vec{k}_i) = \frac{1}{4\pi^2}\iint_{-\infty}^{+\infty} \vec{H}_{FO}(k_x,k_y,\vec{k}_i)e^{j\vec{k}_\rho\cdot\vec{\rho}}dk_xdk_y \quad (1b)$$

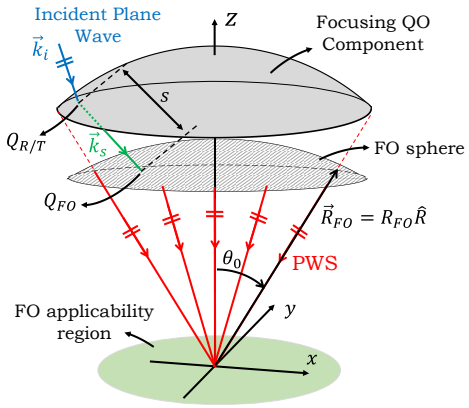


Fig. 3 Schematic representation of a FO scenario for a QO component illuminated by a plane wave from $\hat{k}_i$ direction. A GO propagation scenario is also depicted: the plane wave is scattered by the QO component and propagated to the FO sphere.

where $\vec{\rho}$ is a position on the focal plane of the QO component, $\vec{k}_\rho$ is the spectral vector defined as $\vec{k}_\rho = k_x\hat{x} + k_y\hat{y} = k\sin\theta\,(\cos\phi\,\hat{x} + \sin\phi\,\hat{y})$, and $k$ is the wavenumber in the medium of the focal plane. The dependency of the parameters in (1) from the direction of the incident plane wave is shown explicitly by the term $\vec{k}_i$. The focal fields, $\vec{e}_f$ and $\vec{h}_f$, are expressed as a summation of plane waves with amplitudes of $\vec{E}_{FO}(k_x,k_y,\vec{k}_i)$ and $\vec{H}_{FO}(k_x,k_y,\vec{k}_i)$, respectively. In other words, $\vec{E}_{FO}$ and $\vec{H}_{FO}$ are the PWS representations of $\vec{e}_f$ and $\vec{h}_f$, respectively. The approximations taken to derive (1) are applicable for a region around the centre of the FO sphere. This region, shown in Fig. 3, is a function of the geometrical parameters of the considered scenario, as derived in [20]:

$$D_{FO} = f_\# \min\left(0.4D, \sqrt{2f_\# D\lambda}\right) \quad (2)$$

where $D_{FO}$ is the diameter of a circle in the focal plane which represents the FO applicability region; $\lambda$ is the wavelength in the medium; $D$ and $f_\#$ are the diameter and f-number of the QO component, respectively. The latter is uniformly defined for all components as the ratio between the maximum realizable radius of a FO sphere and diameter of the component, i.e. $f_\# = R_{FO}/D$. This radius, $R_{FO}$, is equal to the focal length, $f$, for parabolic reflectors and hyperbolic lenses; and equal to $0.5D/\sin\theta_0$ for elliptical and extended hemispherical lenses.

The electric PWS in (1a) can be expressed as a function of the electric field scattered by the QO component and evaluated over the FO sphere [27]:

$$\vec{E}_{FO}(k_x,k_y,\vec{k}_i) = \frac{j2\pi R_{FO}e^{-jkR_{FO}}}{\sqrt{k^2-(k_x^2+k_y^2)}}\hat{R}\times\left[\vec{E}_{GO}(k_x,k_y,\vec{k}_i)\times\hat{R}\right] \quad (3)$$

where $\hat{R} = \hat{k}_\rho + \sqrt{1-k_\rho^2/k^2}\,\hat{z}$, and $\hat{R}\times\left[\vec{E}_{GO}(\vec{R})\times\hat{R}\right]$ is the tangent component of the GO field scattered by the QO component and evaluated over the FO sphere. For most practical cases, we can assume the GO field behaves locally as a plane wave and approximate the GO propagation unit vector as $-\hat{R}$. As a consequence, the magnetic PWS in (1b) can be expressed as $\vec{H}_{FO} \approx -1/\zeta\,\hat{R}\times\vec{E}_{FO}$, where $\zeta$ is the characteristic impedance of the medium where the FO sphere is located. As it can be seen in (3), the PWS is proportional to the GO field evaluated over the FO sphere. Therefore, the focus of the following section is on calculating these GO fields for different QO components.

## III. Geometrical Optics Representation of the Fields Scattered to the Fourier Optics Sphere

As mentioned in Sec. II, the field scattered by the QO surface and propagated to the FO sphere, i.e. $\vec{E}_{GO}$, can be evaluated resorting to a GO based analysis. The GO method is commonly used in high-frequency scattering scenarios, i.e. when the scatterers are large in terms of wavelength, to determine wave propagation for both incident and scattered fields, including amplitude, phase, and polarization information. This method is applicable for generic incident fields and scattering surfaces far from the focus (or in general caustics) point. In this method, electromagnetic (EM) waves can be approximated as tubes of rays propagating in a homogenous medium from one point to another. The scattered ray fields follow the laws of reflection and refraction at a two-media interface. In the following, a numerical GO code for calculating $\vec{E}_{GO}$ is described. An analytical expression is also provided for cases when the QO component is illuminated by plane waves with slightly skewed incident angles. This GO field is either integrated to obtain the focal field of the QO component, or directly employed to determine the reception pattern of a QO antenna. Therefore, the accuracy of the former case is dominated by the one of the FO (2), while in the latter case it is comparable to the one of PO method.

Let us assume an incident plane wave, $\vec{E}_i = (E_0^{TE}\hat{p}_i^{TE} + E_0^{TM}\hat{p}_i^{TM})e^{-j\vec{k}_i\cdot\vec{r}}$, is illuminating a QO surface (see Fig. 3), where $\hat{p}_i^{TE/TM} = p_{ix}^{TE/TM}\hat{x} + p_{iy}^{TE/TM}\hat{y} + p_{iz}^{TE/TM}\hat{z}$ represent the TE and TM polarized unit vectors of the incident field, respectively; $E_0^{TE}$ and $E_0^{TM}$ represent the amplitude of the TE and TM polarized fields, respectively. The scattered GO field (reflected or transmitted) on the QO surface, $\vec{E}_s(Q_{R/T})$, can be calculated as:

$$\vec{E}_s(Q_R) = \vec{E}_i\cdot\bar{R}(Q_R) \quad (4a)$$

$$\vec{E}_s(Q_T) = \vec{E}_i\cdot\bar{T}(Q_T) \quad (4b)$$

where $Q_{R/T}$ represents a reflecting surface ($Q_R$) such as a parabolic reflector or a transmitting one ($Q_T$) such as a lens; $\bar{R} = \Gamma^{TE}\hat{p}_i^{TE}\hat{p}_r^{TE} + \Gamma^{TM}\hat{p}_i^{TM}\hat{p}_r^{TM}$ and $\bar{T} = \tau^{TE}\hat{p}_i^{TE}\hat{p}_t^{TE} + \tau^{TM}\hat{p}_i^{TM}\hat{p}_t^{TM}$ are the reflection and transmission dyads, respectively. Here $\Gamma^{TE}$ and $\Gamma^{TM}$ are the TE and TM reflection coefficients on the QO surface; $\tau^{TE}$ and $\tau^{TM}$ are the transmission ones; $\hat{p}_r^{TE/TM}$ and $\hat{p}_t^{TE/TM}$ represent the polarization unit vectors of the reflected and transmitted rays, respectively.

In this work, a ray tracing code is developed which launches incident rays toward a QO component. These rays are scattered by the component and propagated toward the surface of the FO sphere. The propagation directions of the reflected and transmitted rays, $\hat{k}_r$ and $\hat{k}_t$, respectively, are calculated using the vectorial representation of the Snell's law as follows:

$$\hat{k}_r = \hat{k}_i - 2(\hat{k}_i \cdot \hat{n})\hat{n} \quad (5a)$$

$$\hat{k}_t = \frac{\hat{k}_i}{\sqrt{\varepsilon_t}} - \frac{1}{\sqrt{\varepsilon_t}}\left[(\hat{k}_i \cdot \hat{n}) + \sqrt{\varepsilon_t - \left[1 - (\hat{k}_i \cdot \hat{n})^2\right]}\right]\hat{n} \quad (5b)$$

Equations (5a) and (5b) are independent from a specific reference system, and depend only on the material properties, $\varepsilon_t$, the normal vector of the surface, $\hat{n}$, which is pointing toward the medium where the plane wave impinges from, and the direction of incidence wave, $\hat{k}_i$.The position where each ray intercepts with the FO sphere, $Q_{FO}$, is obtained using this ray tracing code, see Fig. 3. In scenarios with a very skewed incident plane wave angle, scattered rays can be intercepted by the FO sphere outside the geometrical maximum rim elevation angle of the QO components ($\theta_0$ in Fig. 3). As a result, FO spheres are not necessarily limited within this angular region. The reflected or transmitted fields evaluated over this FO sphere can be expressed as:

$$\vec{E}_{GO}(Q_{FO}) = \vec{E}_s(Q_{R/T})\, S_{spread}(Q_{FO}) e^{-jks(Q_{FO})} \quad (6)$$

where $s$ is the propagation distance from the QO surface to the FO sphere (see Fig. 3), and $e^{-jks}$ represents the phase propagation for each ray. The amplitude of the GO field spreads as the ray propagates. This spreading is represented by $S_{spread}$ in (6). In the analysed scenarios, this parameter can be evaluated by enforcing the law of conservation of energy among the incident, reflected, and transmitted rays. In other words, when an incident EM field interacts with a QO surface, the power carried by the incident ray tube is equal to the summation of the power reflected back plus the one transmitted into the surface. In a ray picture scenario, far from the focus point (or caustics), one can asymptotically evaluate the PO radiation integral to derive a GO representation of the EM fields. The spreading factor is then computed using this method as described in [27] and [29]:

$$S_{spread}(Q_{FO}) = \sqrt{\frac{\rho_1^{r/t}(Q_{FO})\rho_2^{r/t}(Q_{FO})}{\left(\rho_1^{r/t}(Q_{FO})+s(Q_{FO})\right)\left(\rho_2^{r/t}(Q_{FO})+s(Q_{FO})\right)}} \quad (7)$$

where $\rho_1^{r/t}$ and $\rho_2^{r/t}$ are the principal radii of curvature of the reflected or transmitted wave fronts, respectively. In the case of an arbitrary astigmatic incident wave front, these radii are computed for transmission or reflections scenarios in [29].

The GO field calculated in (6) is a function of the position where the scattered rays intercepted by the FO sphere, $Q_{FO}$. However, as indicated in (3), the GO field should be represented as a function of the spectral parameters, i.e. $k_x$ and $k_y$. This change of variables is achieved by employing a standard interpolation code (using "griddata" function) in MATLAB.

For the listed QO components, when illuminated by a plane wave from broadside direction, we also derived the corresponding analytical representation of the amplitude spreading factors, as shown in Table I. In this table, for the elliptical lens, $2a$ is the major axis, $2c$ is the distance between the foci, $e = c/a$ is its eccentricity, and $R_{FO}$ is the rim distance from the lower focus of the lens to its edge. For a hyperbolic lens, $e$ represents its eccentricity. The geometrical parameters of each QO component are shown in Fig. 4.

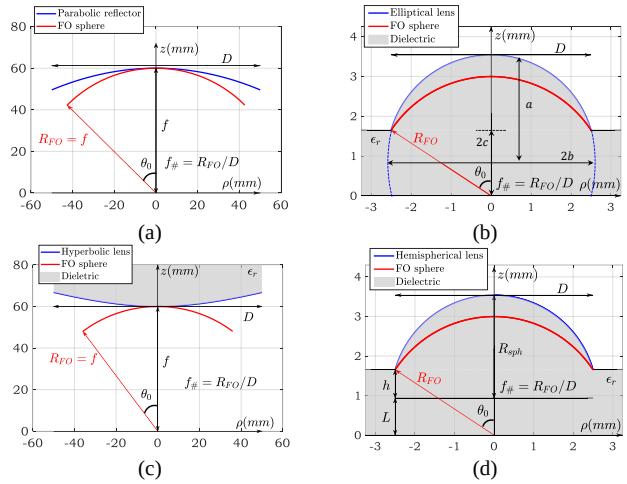


Fig. 4 Geometrical parameters of the considered QO components. (a) Parabolic reflector, (b) elliptical, (c) hyperbolic, and (d) extended hemispherical lenses.

TABLE I. ANALYTICAL SPREADING FOR QUASI-OPTICAL COMPONENTS ILLUMINATED BY A PLANE WAVE FROM BROADSIDE DIRECTION

| QO component | Broadside Spreading Factor: $S_{spread}(\theta, \theta_i = 0)$ |
|---|---|
| Parabolic reflector | $2/(1+\cos\theta)$ |
| Elliptical lens | $a(1-e^2)/\left(R_{FO}(1-e\cos\theta)\right)$ |
| Hyperbolic lens | $(1-e)/(1-e\cos\theta)$ |

Moreover, the phase term, $e^{-jks}$, in (6) can also be represented analytically for specific cases. In the case of broadside illumination of a parabolic reflector, due to its geometrical shape, the reflected GO field has a constant phase over its FO sphere. Similarly, for elliptical lenses and hyperbolic lenses, their eccentricities are chosen in such a way to ensure constant phase fronts for transmitted fields over their corresponding FO spheres when illuminated by a plane wave from the broadside direction. These eccentricities are $e = 1/\sqrt{\varepsilon_r}$ and $e = \sqrt{\varepsilon_r}$, for elliptical and hyperbolic lenses,

respectively, where $\varepsilon_r$ is the relative permittivity of the lens material. Therefore, for broadside incidence and the considered canonical QO components, one can neglect the constant phase terms of the reflected or transmitted GO fields over their FO spheres in the analysis of the scenario.

As described in [21], when the incident skew angle of the plane wave, $\theta_i$, is less than $11^\circ$, one can assume that the polarization of the incident field $\vec{E}_i$ remains the same as the broadside one, committing at most 20% error. Moreover, the phase of the incident field coming from a skew angle can be approximated by a progressive phase shift. This phase term is caused by the transversal propagation of the incident plane wave. This progressive phase shift includes a linear phase term, $e^{-j\vec{k}_\rho\cdot\vec{\rho}_{fp}}$, and a coma phase term, $e^{-j\vec{k}_\rho\cdot\vec{\rho}_{fp}\delta_n}$, where $\delta_n(\theta) = \delta(\theta)/R_{FO}$ (Table II), $\delta(\theta)$ represents the geometrical distance from a QO surface to its FO sphere with maximum possible radius $R_{FO}$, and $\vec{\rho}_{fp} = R_{FO}\vec{k}_{\rho i}/k$ is referred to as the flash point position. This position indicates geometrically where on the focal plane, the focused field would be maximum (assuming beam deviation factor is 1); and $\vec{k}_{\rho i} = k\sin\theta_i\,\hat{\rho}$ is the transversal component of the incident wave vector. Therefore, the linear phase term corresponds to steering the main beam of the focal field from the centre of the focal plane to the flash point position. While the coma phase term leads to the deviation of the main beam, which is related to the parameter $\delta_n(\theta)$ [21]. To conclude, the GO representation of the scattered fields evaluated over the FO sphere, for slightly off-broadside plane wave incidences, can be expressed analytically as:

$$\vec{E}_{GO}(\theta,\theta_i) \simeq \vec{E}_s(\theta,\theta_i=0)S_{spread}(\theta,\theta_i=0) \cdot e^{-j\vec{k}_\rho\cdot\vec{\rho}_{fp}(\theta_i)(1+\delta_n(\theta))} \quad (8)$$

Similarly to the case in (6), the GO fields calculated in (8) are also interpolated to be represented as a function of spectral parameters.

TABLE II. NORMALIZED DISTANCE BETWEEN QUASI-OPTICAL COMPONENTS AND THEIR CORRESPONDING FO SPHERES

| QO component | Normalized distance $\delta_n(\theta)$ |
|---|---|
| Parabolic reflector | $\frac{1-\cos\theta}{1+\cos\theta}$ |
| Elliptical lens | $\frac{e(\cos\theta-\cos\theta_0)}{1-e\cos\theta}$ |
| Hyperbolic lens | $\frac{e(\cos\theta-1)}{1-e\cos\theta}$ |

In the presented tool, for incident angles less than 11 degrees, i.e. $\theta_i \le 11^\circ$, the analytical solution in (8), using the analytical spreading factors in Table I, is implemented. For larger incident angles, the numerical solution in (6), using the numerical spreading factor (7), is employed. Since an analytical expression is not available for the extended hemispherical lenses, in their case, only the numerical GO representation is implemented.

*Numerical Examples*

In the following, firstly the GO fields for different QO components are shown and compared. We divided the QO components into two sets: components which are very large in terms of the wavelength, see Fig. 5, parabolic reflector and hyperbolic lens ($\varepsilon_r = 2.4$), respectively; and components comparable in size to the wavelength, see Fig. 6, elliptical and extended hemispherical lenses ($\varepsilon_r = 11.9$), respectively. The operative frequency is 300 GHz, the plane wave is TM polarized, and for all components the f-number is 0.6. For the reflector and the hyperbolic lens, the diameter is chosen as 100 mm, and the incident skew angle is $\theta_i = 8^\circ$, which allows us to use the analytical solution in (8). As it can be seen, for the hyperbolic lens, both the amplitude and phase terms of the GO field vary more significantly with respect to the ones of the parabolic reflector. In the case of the elliptical and extended hemispherical lenses, the diameter is 5 mm, and the skew angle is $\theta_i = 21^\circ$ (numerical solution in (6) is used). The radius of the hemisphere and the extension length of the hemispherical lens are $R_{sph} = 2.6$ mm, and $L = 0.362R_{sph}$, respectively. It can be seen that for the chosen lenses, their GO fields are almost equal due to their similar lens shapes. Moreover, since the incident plane wave angle is very skewed, part of the lens surface is obscured from the incident plane wave. This shadow region is highlighted in the inset of Fig. 6.

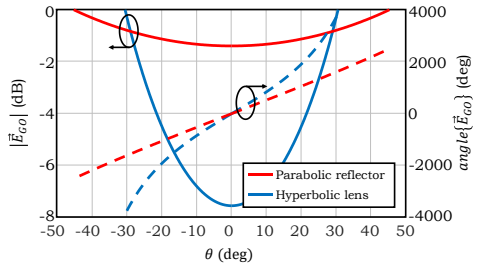


Fig. 5 GO fields of a parabolic reflector and a hyperbolic lens. These fields are evaluated at $\phi = 0^\circ$ plane, using the analytical expression in (8). The amplitude and phase terms are plotted using the left and right axes, respectively. The diameter and f-number of both components are $D^r = D^h = 100$ mm and $f_\#^r = f_\#^h = 0.6$, respectively. The incident plane wave is TM polarized operating at 300 GHz with the skew angle of $\theta_i = 8^\circ, \phi_i = 0^\circ$. For the hyperbolic lens, the permittivity of the dielectric is $\varepsilon_r = 2.4$.

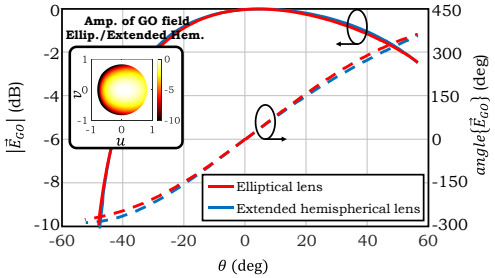


Fig. 6 GO fields of an elliptical lens and an extended hemispherical lens. These fields are evaluated at $\phi = 0^\circ$ plane, using the numerical expression in (6). The amplitude and phase terms are plotted using the left and right axes, respectively. The diameter and f-number of both components are $D^l = 5$ mm and $f_\#^l = 0.6$, respectively. The incident plane wave is TM polarized operating at 300 GHz with the skew angle of $\theta_i = 21^\circ, \phi_i = 0^\circ$. The permittivity of the dielectric is $\varepsilon_r = 11.9$. The shadow region is visible in the 2-D amplitude figure at the left side of the lens surfaces.

In the remaining parts of this sub-section, the GO fields calculated by the tool are indirectly validated by resorting to full-wave simulations similarly to [20]. In particular, we calculated the focal fields of QO components using (1). For the case of a hyperbolic lens, these fields are compared against the ones evaluated using the PO based code of GRASP simulation software [18], and for an elliptical lens using CST [28].

First let us consider the same hyperbolic lens as in Fig. 5, which is now illuminated by an incident plane wave with an incident skew angle of $\theta_i = 1.3°, \phi_i = 0°$. In Fig. 7, the amplitude and phase of the x-component of the focal electric field calculated by using the analytical GOFO analysis, as in (1), (3), and (8), are compared against PO results. As it can be seen, the agreement between the two methods, both in the amplitude and phase, is very good within the FO applicability region (2).

As another example, we consider the same elliptical lens as in Fig. 6, which is now illuminated by plane waves with two incident skew angles. As it can be seen in Fig. 8(a) and (b), for the case of plane wave illumination with the incident angle of $\theta_i = 8°$ and $\phi_i = 0°$, the amplitude and phase terms of the focal field evaluated by analytical GOFO method are in very good agreement with the results reported by CST within the FO applicability region.

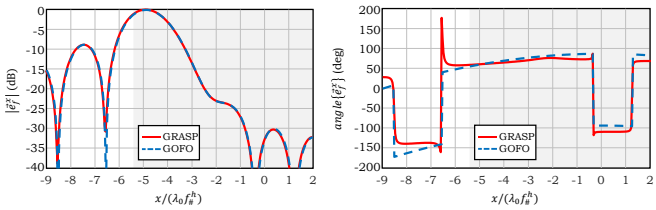


(a) (b)

Fig. 7 x-component of the electric field on the focal plane of a hyperbolic lens, same as the one in Fig. 5, illuminated by a plane wave with an incident angle of $\theta_i = 1.3°, \phi_i = 0°$. The field is evaluated at $y_f = 0$ plane, calculated using the analytical GOFO approach, as in (1), (3), and (8), and is compared against the one obtained using the PO based code of GRASP: (a) Amplitude. (b) Phase. The grey region represents the FO applicability region in (2).

In the case of a plane wave illumination with the incident angle of $\theta_i = 21°$ and $\phi_i = 0°$, the analytical GO approximation is not valid anymore ($\theta_i > 11°$). Therefore, the numerical GO approach in (6) is employed. Here, the results from the GOFO approach are also in good agreement with the CST results within the FO applicability region, as shown in Fig. 8(c) and (d). However, since a considerable portion of the power at the focal plane is focused outside this applicability region, another approach is also employed here to indirectly validate the GO code. Namely, a GOPO approach, where the scattered field is still calculated over the FO sphere using the numerical GO approach, and then a PO radiation integral is used to calculate the field at the focal plane of the elliptical lens. As it can be seen, the amplitude and phase of the focal field calculated using the GOPO approach are also in good agreement with the results reported by CST outside the FO applicability region.

The GO fields of the remaining QO components are also validated in a similar manner. In the following section, these GO fields are used to analyse the reception properties of antenna feeds coupled to these QO components.

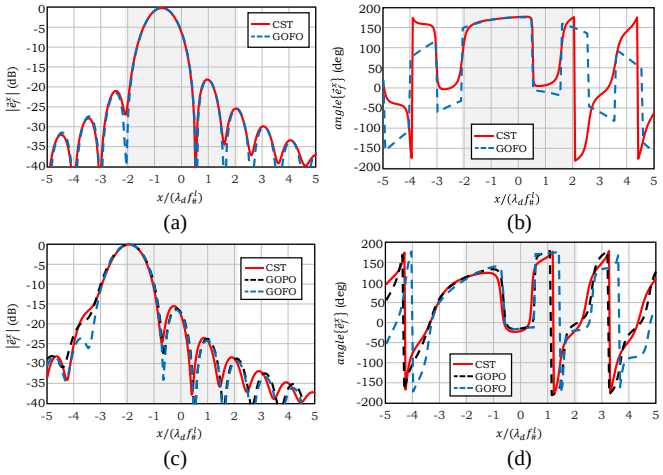


(a) (b)

(c) (d)

Fig. 8 x-component of the electric field on the focal plane of an elliptical lens, same as the one in Fig. 6. The field is evaluated at $y_f = 0$ plane, calculated using the analytical or numerical GOFO approaches, and compared against the one obtained from CST. In the case of $\theta_i = 8°, \phi_i = 0°$, (a) amplitude and (b) phase. In the case of $\theta_i = 21°, \phi_i = 0°$, (c) amplitude and (d) phase. The grey region represents the FO applicability region in (2).

## IV. Antenna-Coupled Quasi-Optical Systems

The developed GUI, see Fig. 1, is capable of analysing the coupling of antenna feeds to QO components in reception. By taking the pattern of an antenna feed on a spherical surface as input, the tool evaluates the performance of this feed coupled to a specific QO component. This performance is reported in terms of the far-field pattern, efficiency terms, directivity and gain.

Let us assume a reception scenario where an incident plane wave, coming from $\vec{k}_i$ direction, illuminates a QO component, as depicted in Fig. 9. This field is then scattered by the QO surface and captured by a feeding antenna which is placed at the focal plane of the QO component. In [22], the power received by the feed of a reflector antenna (assuming impedance matching condition) is estimated using the open-circuit voltage in a Thévenin equivalent circuit. This voltage, $V_{oc}$, is calculated as a reaction integral between the equivalent currents radiated by the feed, without the presence of the QO component, and the incident ones coming from the QO component. Both of these currents are evaluated over an arbitrary surface between the feed and the QO component. In [16] and [23], this procedure is linked to the FO representation of the fields radiated by a QO component. Here, incident equivalent currents are obtained on the FO sphere using the previously derived PWS fields, and the ones radiated by the feed are obtained by propagating the fields of the feed given by the user to the FO sphere. If we approximate the incident PWS of the QO component described in (1b) as $\vec{H}_{FO} \approx -1/\zeta\, \hat{R} \times$

$\vec{E}_{FO}$, the open-circuit voltage, $V_{oc}(\vec{k}_i)$, can be evaluated as follows:

$$V_{oc}(\vec{k}_i)I_0 = \frac{-jR_{FO}e^{jkR_{FO}}}{2\pi k}$$

$$\iint_{\Omega_{FO}} \left(\frac{1}{\zeta}\vec{E}_a^{Tx}\cdot\vec{E}_{FO} - \zeta\vec{H}_a^{Tx}\cdot\vec{H}_{FO}\right)dk_x dk_y \quad (9)$$

where $\Omega_{FO}$ is the domain of integration which covers the entire angular region subtended by the FO sphere; $\vec{E}_a^{Tx}(\vec{k}_\rho)$ and $\vec{H}_a^{Tx}(\vec{k}_\rho)$ are the EM fields radiated by the antenna feed in Tx into the FO sphere, when fed by a current of amplitude $I_0$. The dependency of $\vec{k}_i$ in (9) comes from $\vec{E}_{FO}(\vec{k}_\rho,\vec{k}_i)$ and $\vec{H}_{FO}(\vec{k}_\rho,\vec{k}_i)$. Note that (2) represents the applicability region for calculating the focal fields, (1), using the PWS; however, it does not indicate the validity of the method in evaluating the GO fields as well as the results obtained using (9). By using the open-circuit voltage in (9), the power delivered to the load of the feed (assuming impedance matching condition), $P_L(\vec{k}_i)$, can be expressed as:

$$P_L(\vec{k}_i) = \frac{\left|V_{oc}(\vec{k}_i)I_0\right|^2}{16\,P_{rad}} \quad (10)$$

where $P_{rad}$ is the total power radiated by the feed in Tx. As it can be concluded by (9) and (10), to maximize the power delivered to the load of a feed, the fields radiated by the feed should be synthesized as the conjugate of the incident PWS.

The tool imports the fields radiated by an antenna feed, $\vec{E}_a^{Tx}$, from external files with GRASP format (such as the ones generated by CST) or from MATLAB matrices (Fig. 1). A user provides the spherical components of $\vec{E}_a^{Tx}(\vec{R}_a)$ evaluated over a full hemisphere with radius $R_a$ centred at the phase centre of the feed (Fig. 9). Moreover, the user defines the polarization and location, $\vec{d}_a$, of the feed in the focal plane (Fig. 9). The tool first coverts $\vec{E}_a^{Tx}(\vec{R}_a)$ from spherical coordinates to cartesian coordinates. It then propagates $\vec{E}_a^{Tx}(\vec{R}_a)$ backward and forward from the user-defined sphere to the FO sphere as follows (assuming that both spheres are in far-field distance from the feed):

$$\vec{E}_a^{Tx}(\vec{k}_\rho) = \vec{E}_a^{Tx}(\theta_a\rightarrow\theta')\frac{R_a e^{jkR_a}e^{-jkR'_{FO}}}{R'_{FO}} \quad (11)$$

where $R'_{FO}(\vec{k}_\rho)$ is the distance from $\vec{d}_a$ to the FO sphere and $\vec{E}_a^{Tx}(\theta_a\rightarrow\theta')$ represents the interpolation process to relate the angular parametrization of the two spheres as shown in Fig. 9. The magnetic field is approximated from the electric field on the user-defined sphere as $\vec{H}_a^{Tx}(\vec{R}_a)\approx 1/\zeta\hat{R}_a\times\vec{E}_a^{Tx}(\vec{R}_a)$. Following similar steps as in (11), $\vec{H}_a^{Tx}(\vec{k}_\rho)$ can be obtained. In order to compare the incident PWS and the fields radiated by the feed and to determine whether the conjugate field matching condition is satisfied, the user can plot $\vec{E}_a^{Tx}(\vec{k}_\rho)$ and $\vec{H}_a^{Tx}(\vec{k}_\rho)$ using the "Plot" button shown in Fig. 1. In cases that the FO sphere is in the near-field distance from the feed, the user can provide the near fields, $\vec{E}_a^{Tx}$ and $\vec{H}_a^{Tx}$, directly on the FO sphere using MATLAB matrices.

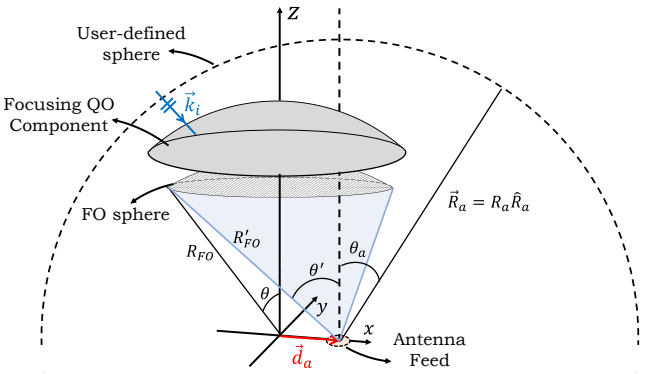


Fig. 9 Antenna in Rx scenario. An antenna feed is placed at a certain position, $\vec{d}_a$, in the focal plane of the focusing component. The blue region represents the portion of the radiated field captured by the FO sphere.

Once the power delivered to the load of the feed, $P_L$, is calculated, efficiency terms, directivity, and gain in reception can be computed and displayed by the GUI as a function of the incident plane wave direction. The aperture efficiency in Rx is evaluated as the ratio between the delivered power, $P_L$, and the incident power captured by the QO component, $P_{inc}$, as: $\eta_{ap}^{Rx}(\vec{k}_i) = P_L(\vec{k}_i)/P_{inc}$, where $P_{inc} = 0.5|E_0|^2A_{QO}/\zeta$, and $A_{QO}$ is the physical area of the QO component. The spillover efficiency in Rx, $\eta_{so}^{Rx}$, is evaluated using the same method as in Tx. For reflectors and hyperbolic lenses, it is defined as the ratio between the power radiated by the feed and captured by the FO sphere, and the total power radiated by the feed, $P_{rad}$; while for elliptical and hemispherical lenses, it is obtained as the ratio between the power transmitted outside the lens surface (i.e. including reflection/transmission at the surface), and $P_{rad}$. The taper efficiency is then obtained as: $\eta_t^{Rx} = \eta_{ap}^{Rx}/\eta_{so}^{Rx}$. Once these efficiency terms are calculated, the directivity and gain of the system are represented in Rx as: $D^{Rx}(\vec{k}_i) = D^{max}\eta_t^{Rx}(\vec{k}_i)$, and $G^{Rx}(\vec{k}_i) = D^{max}\eta_{ap}^{Rx}(\vec{k}_i)$, respectively, where $D^{max} = (4\pi/\lambda^2)A_{QO}$ is the maximum achievable directivity for a given size of the QO component.

By using reciprocity, the electric field, $\vec{E}_{QO}$, that the antenna-coupled QO system would radiate to $(R_{FF},\theta_{FF},\phi_{FF})$ position, at a far distance from the QO component, is evaluated as [27]:

$$\vec{E}_{QO}(R_{FF},\theta_{FF},\phi_{FF}) = \frac{k\zeta I_0}{E_0}$$
$$\left(V_{oc}^{TM}(\theta_{FF},\phi_{FF})\hat{\theta} + V_{oc}^{TE}(\theta_{FF},\phi_{FF})\hat{\phi}\right)\frac{e^{-jk_0R_{FF}}}{4\pi R_{FF}} \quad (12)$$

where $E_0$ is the amplitude of the incident plane wave; and $V_{oc}^{TE/TM}$ are the induced TE and TM polarized Thévenin open-circuit voltages in (9), respectively. These voltages are evaluated using (9) when the QO component is illuminated by TE/TM polarized incident plane waves from the direction $\theta_i = \theta_{FF}$ and $\phi_i = \phi_{FF}$.

In order to construct the pattern in Rx, one needs to illuminate the QO component by a set of incident fields with different skew angles: $\theta_{FF} \in [0, \theta_{Rx}]$ , $\phi_{FF} \in [0, 2\pi]$ , where $\theta_{Rx}$ represents the maximum elevation angle in the observation grid. By using (12), the GUI plots and exports both the amplitude and phase of the radiative pattern ("Export" button in Fig. 1). It is worth noting that evaluating this radiative pattern of the whole QO system in Rx is a slower process with respect to the analysis in Tx, especially for cases when $\theta_{Rx} > 11°$ , where the numerical GO, (6), and related interpolation codes should be employed to calculate this pattern. The main purpose of the GUI is to design feeds for QO systems by matching their radiated fields to the incident PWS. The GUI performs fast when deriving the incident PWS as well as calculating the aperture efficiency, directivity and gain of the antenna-coupled QO systems per incident direction.

*Numerical Examples*

In this subsection, the performance of antenna feeds coupled to QO systems are evaluated in Rx, and compared against the ones obtained in a conventional transmission mode. The proposed tool is capable of analysing the performance in a desired frequency band. Here for simplicity, we only showed the results corresponding to a single frequency. Let us first consider a case of an integrated lens antenna with a Gaussian antenna feed displaced by $\vec{d}_l$ from the focus of an elliptical silicon lens ($\varepsilon_r = 11.9$) as shown in Fig. 10a. To improve the transmission at the silicon-air interface, the lens surface is covered by a quarter-wavelength Anti-Reflection (AR) coating made of Parylene with the relative permittivity of $\varepsilon_m = 2.62$. This layer is analysed in the code using a transmission line model of the stratification. The frequency of operation is 300 GHz. The Gaussian feed parameters are designed in such a way that the far field of the feed is symmetric and has $-11$ dB field taper at the edge of the lens surface. The lens has a diameter of $D^l = 5$ mm, and a rim angle of $\theta_0^l \simeq 56°$ (corresponding to $f_\#^l = 0.6$). In this example scenario, the feed is displaced by $\vec{d}_l = 0$ and $0.348\hat{x}$ mm from the lower focus of the lens. These displacements correspond to scanning the radiation pattern by 0 (broadside) and 2 beams (3 dB overlapping beams) with respect to the broadside direction, respectively, i.e. the main beam is pointing to $\theta_{FF} = 0°$ and 21°, respectively, and $\phi_{FF} = 180°$.

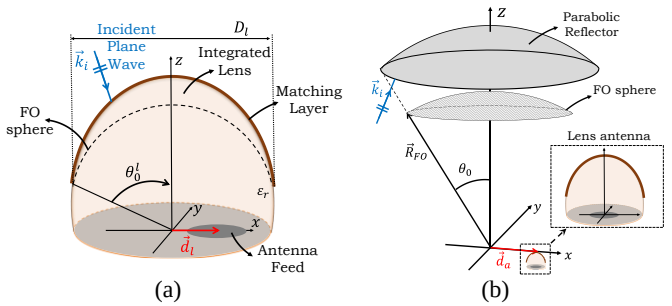


Fig. 10 (a) Antenna-coupled elliptical silicon lens implemented with a matching layer. The feed is displaced by $\vec{d}_l$ from the lower focus of the lens. (b) Lens antenna coupled to a parabolic reflector. The antenna is displaced by $\vec{d}_a$ from the focus of the reflector.

For the described configuration, the analysis performed in Rx is compared to the one in Tx. The radiative patterns are compared in Fig. 11. The analysis in Tx is performed by using an in-house PO code which is validated by CST full-wave simulation. As it can be seen in the figure, the patterns in Rx in both cases are in good agreement with the ones obtained in Tx. In the Tx analysis, the field radiated by the antenna is propagated out of the lens (taking into account the effect of the matching layer). This field is evaluated outside the lens surface and shown for the case of scanning 2 beams in the inset of Fig. 11(b). As it can be seen, the large scanning angle in this case leads to total reflection from a considerable portion of the lens surface. In such an extreme case, when the angle of rays inside the lens approaches the critical angle, a transition field is present at the lens interface, which has to correct the GO field to properly reconstruct the total field [30]. However, in the in-house PO code and Rx tool such a transition field is not considered. We assume the fields in this shadow region are zero. The aperture efficiency, directivity and gain evaluated in Rx are also compared against the ones obtained in Tx for both cases with very good agreement, as shown in Table III.

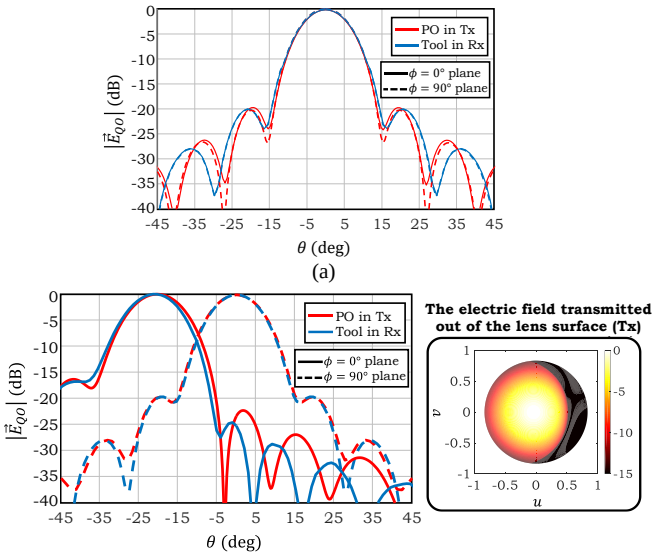


Fig. 11 Amplitude of the radiative co-pol. pattern of a lens antenna with a Gaussian feed: (a) scanning to broadside direction, and (b) scanning 2 beams, i.e. pointing the main beam to $\theta_{FF} = 21°$ and $\phi_{FF} = 180°$. Inset in (b) shows the electric field transmitted out of the integrated lens and evaluated on its surface in Tx.

TABLE III. PERFORMANCE OF THE DESCRIBED ANTENNA-COUPLED ELLIPTICAL LENS

| Analysis in Tx/Rx | Aperture Eff. | Directivity | Gain |
|---|---|---|---|
| Broadside | 80.7%/79.9 % | 23.8/23.7 dB | 23.0/22.9 dB |
| Scanning 2 beam | 56.9%/60.5 % | 23.0/23.4 dB | 21.5/21.7 dB |

In order to demonstrate the capability of the tool in analysing geometries with realistic feeds, we now present the results with a leaky-wave feed antenna as in [31]. The considered scenario

is the same as the one in Fig. 11. In this case the feed is displaced by $\vec{d}_l = 0$ and $-0.348\hat{x}$ mm. The field from the leaky-wave feed has also similar taper level to the one of the Gaussian feed in Fig. 11. The geometrical parameters of the designed tapered leaky slot are the following: slot length is $0.8\lambda_0$; tapering angle is 35°; the airgap distance between the lens and the slot ground plane is $0.016\lambda_0$; the initial width and the end width of the slot are $0.005\lambda_0$ and $0.56\lambda_0$, respectively.

For the described configuration, the analysis performed in Rx is compared to CST full-wave simulation done without including multiple reflections. The radiative patterns are compared in Fig. 12. As it can be seen, the Rx and CST analyses are in a very good agreement for both co- and cross-polarizations in broadside and scanning cases (2 beams). The gains obtained in Rx and using CST are both 22.6 dB for the broadside case, whereas 21.8 dB and 21.1 dB for the scanning case, respectively. It can be seen the agreement in scanning gains is a bit worse compared to broadside case. This is because the previously mentioned shadow region and transition fields are not modelled in the Rx tool.

The above-mentioned Tx and Rx analyses have been executed on a workstation PC with a 512 GB of RAM and a CPU with 3.00 GHz clock cycle. The tool in Rx took about 1 min to estimate the gain, while the CST simulations took about 90 mins.

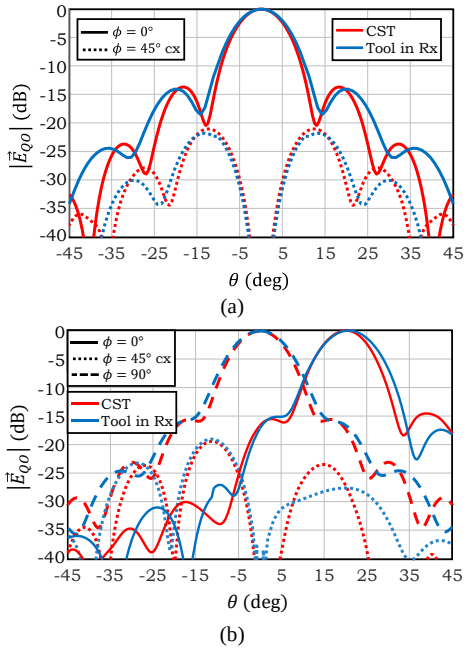


Fig. 12 Amplitude of the radiative co- and cross-polarization patterns of a leaky-lens antenna: (a) scanning to broadside direction, and (b) scanning 2 beams, i.e. pointing the main beam to $\theta_{FF} = 21°$ and $\phi_{FF} = 0°$. Note that the most dominant cross-polarization pattern is along $\phi = 45°$ plane.

As an another example, let us consider a scenario with integrated lens antenna coupled to the rest of the QO chain. For simplification, here this QO chain is modelled by a single on-axis parabolic reflector, as depicted in Fig. 10b. The feed is the entire lens antenna in Fig. 10a. However, in this case, the Gaussian feed is fixed at the lower focus of the elliptical lens, i.e. $|\vec{d}_l| = 0$. The diameter of the reflector is $D^r = 125$ mm, and its f-number is $f_\#^r = 2.6$ ($\theta_0^r \simeq 11°$). The lens antenna is displaced from the centre of the parabola's focal plane by a distance $\vec{d}_a = 13\hat{x}$ mm and $65\hat{x}$ mm for the two considered scanning cases. These displacements correspond to scanning the radiation pattern of the complete QO system by 5 beams and 25 beams (3 dB overlapping beams) with respect to the broadside direction, i.e. the main beam is pointing to $\theta_{FF} = 2.3°$ and $\theta_{FF} = 11.45°$, respectively, and $\phi_{FF} = 0°$.

As shown in Fig. 13, the radiative patterns obtained in Rx are comparable to the ones in Tx. In this example, when calculating the pattern in Rx, the far field radiated by the lens antenna, $\vec{E}_a^{Tx}$, is the field transmitted outside the lens and evaluated at the FO sphere of the reflector. This far field is obtained using the tool (results shown in Fig. 11(a)). The pattern in Tx is obtained by importing the far-field pattern of the lens antenna into GRASP as a tabulated feeding source which illuminates the reflector. In Table IV, the aperture efficiency, directivity, and gain of the lens antenna-coupled reflector, evaluated in Rx, are shown and compared against the ones obtained in Tx with excellent agreement between the two methods.

TABLE IV. PERFORMANCE OF THE DESCRIBED LENS ANTENNA-COUPLED PARABOLIC REFLECTOR

| Analysis in Tx/Rx | Aperture Eff. | Directivity | Gain |
|---|---|---|---|
| Scanning 5 beams | 52.4%/53.0% | 51.3/51.3 dB | 49.1/49.1 dB |
| Scanning 25 beams | 13.2%/12.3% | 49.1/48.9 dB | 43.1/42.8 dB |

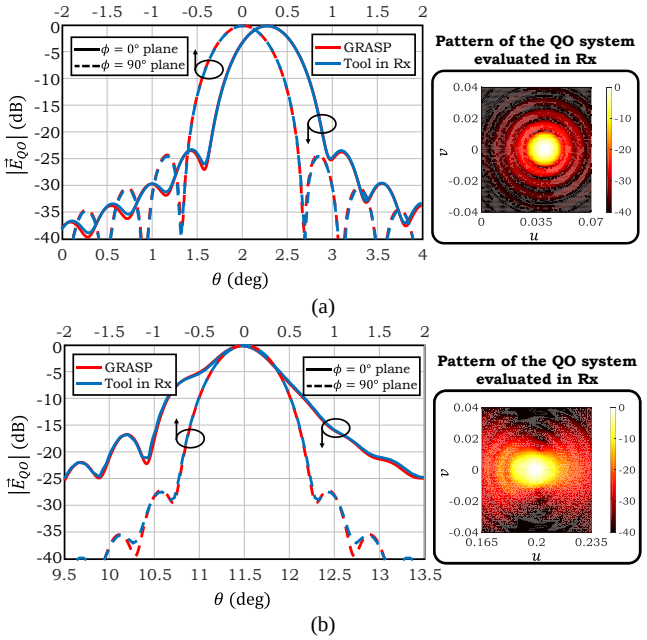


Fig. 13 Amplitude of the radiative co-pol. pattern of the lens antenna-coupled parabolic reflector. (a) Scanning 5 beams, i.e. pointing to $\theta_{FF} = 2.3°$ and $\phi_{FF} = 0°$. (b) Scanning 25 beams, i.e. pointing to $\theta_{FF} = 11.45°$ and $\phi_{FF} = 0°$. The 2-D co-pol. amplitude patterns evaluated in Rx are shown in the insets.

## V. Conclusion

In this article, we introduced a freely accessible software for analysing antenna-coupled QO systems in reception. By using the described field correlation methodology in reception, the geometry of antenna feeds can be designed to match their radiated fields to the incoming PWS. As a result of this technique, one can maximize the aperture efficiencies of a QO system for broadside and/or steering cases. The GUI applies the GOFO analysis for four commonly used QO components to provide more design possibilities to users: parabolic reflectors, elliptical, extended hemispherical, and hyperbolic lenses. The interface of the GUI is informative and simple which allows users, who are less experienced with the described theory, to analyse and design QO based systems.

The GUI is based on evaluating the fields scattered by QO components using a GO representation. These fields are evaluated analytically when possible, and if not, using a numerical approach. Furthermore, for antenna-coupled QO systems, the power delivered to the antenna load is computed by performing a field matching between the incident PWS and the field radiated by the antenna feed. Moreover, the performance of three test scenarios is evaluated using the described reception formalism. The performance criteria reported by the GUI are based on the radiative pattern, aperture efficiency, directivity, and gain of the system. The tool is validated by full-wave simulations with excellent agreement.

## References


[1] M. Calvo, et al., "The NIKA2 instrument, a dual-band kilopixel KID array for millimetric astronomy," *J. Low Temp. Phys.*, vol. 184, no. 3, pp. 816–823, Aug. 2016.

[2] Gordon J. Stacey, et. al, "SWCam: the short wavelength camera for the CCAT Observatory," *SPIE Millimeter, Submillimeter, and Far-Infrared Detectors and Instrumentation for Astronomy VII*, vol. 9153, pp. 165–180, 2014.

[3] J. Baselmans, et al., "A kilo-pixel imaging system for future space based far-infrared observatories using microwave kinetic inductance detectors," *Astronomy & Astrophysics*, vol. 601, p. A89, 2017.

[4] L. Ferrari, et al., "Antenna coupled MKID performance verification at 850 GHz for large format astrophysics arrays," *IEEE Trans. on Terahertz Sci. and Tech.*, vol. 8, no. 1, pp. 127–139, Jan. 2018.

[5] K. B. Cooper, et al., "THz imaging radar for standoff personnel screening," *IEEE Trans. on Terahertz Sci. and Tech.*, vol. 1, no. 1, pp. 169–182, 2011.

[6] S. Rowe, et al., "A passive terahertz video camera based on lumped element kinetic inductance detectors," *AIP Review of Scientific Instruments*, vol. no. 3, pp. 033105, Mar. 2016.

[7] E. Gandini, J. Svedin, T. Bryllert and N. Llombart, "Optomechanical system design for dual-mode stand-off submillimeter wavelength imagers," *IEEE Trans. on Terahertz Sci. and Tech.*, vol. 7, no. 4, pp. 393–403, July 2017.

[8] S. van Berkel, O. Yurduseven, A. Freni, A. Neto and N. Llombart, "THz imaging using uncooled wideband direct detection focal plane arrays," *IEEE Trans. on Terahertz Sci. and Tech.*, vol. 7, no. 5, pp. 481–492, Sept. 2017.

[9] F. García-Rial, et al., "Combining commercially available active and passive sensors into a millimeter-wave imager for concealed weapon detection," *IEEE Trans. on Microwave Theory and Techniques*, vol. 67, no. 3, pp. 1167–1183, March 2019.

[10] X. Wu, G. V. Eleftheriades and T. E. van Deventer-Perkins, "Design and characterization of single- and multiple-beam mm-wave circularly polarized substrate lens antennas for wireless communications," *IEEE Trans. on Microwave Theory and Techniques*, vol. 49, no. 3, pp. 431–441, March 2001.

[11] G. Godi, R. Sauleau and D. Thouroude, "Performance of reduced size substrate lens antennas for millimeter-wave communications," *IEEE Trans. on Antennas Propag.*, vol. 53, no. 4, pp. 1278–1286, April 2005.

[12] J. Ala-Laurinaho, et al., "2-D beam-steerable integrated lens antenna system for 5g e-band access and backhaul," *IEEE Trans. on Microwave Theory and Techniques*, vol. 64, no. 7, pp. 2244–2255, July 2016.

[13] A. Bisognin et al., "Ball grid array module with integrated shaped lens for 5G backhaul/fronthaul communications in f-band," *IEEE Trans. on Antennas Propag*, vol. 65, no. 12, pp. 6380–6394, Dec. 2017.

[14] T. Jaschke, B. Rohrdantz, H. K. Mitto and A. F. Jacob, "Ultrawideband siw-fed lens antenna," *IEEE Antennas and Wireless Propag. Letters*, vol. 16, pp. 2010–2013, 2017.

[15] A. Artemenko, A. Mozharovskiy, A. Maltsev, R. Maslennikov, A. Sevastyanov and V. Ssorin, "Experimental characterization of e-band two-dimensional electronically beam-steerable integrated lens antennas," *IEEE Antennas and Wireless Propag. Letters*, vol. 12, pp. 1188–1191, 2013.

[16] M. Arias Campo, D. Blanco, S. Bruni, A. Neto and N. Llombart, "On the Use of Fly's Eye Lenses with Leaky-Wave Feeds for Wideband Communications," *IEEE Trans. on Antennas Propag.*, vol. 68, no. 4, pp. 2480-2493, April 2020.

[17] ZEMAX, OpticStudio version 18.9.

[18] TICRA, GRASP Version 10.5.0.

[19] P. Pathak, "High frequency techniques for antenna analysis," *Proceedings of the IEEE*, vol. 80, no. 1, pp. 44–65, 1992.

[20] N. Llombart, et al., "Fourier Optics for the analysis of distributed absorbers under THz focusing systems," *IEEE Trans. on Terahertz Sci. and Tech.*, vol. 5, no. 4, pp. 573–583, 2015.

[21] N. Llombart, et al., "Reception power pattern of distributed absorbers in focal plane arrays: a Fourier Optics analysis," *IEEE Trans. on Antennas Propag.*, vol. 66, no. 11, pp. 5990–6002, 2018.

[22] V. Rumsey, "On the design and performance of feeds for correcting spherical aberration," *IEEE Trans. on Antennas Propag.*, vol. 18, no. 3, pp. 343–351, 1970.

[23] H. Zhang, "A GO/FO Tool for Analyzing Quasi-Optical Systems in Reception," M.S. thesis, Dept. of Microelectronics, Delft Univ. of Technology, the Netherlands, 2018.

[24] O. Yurduseven, N. Llombart, A. Neto, "A dual-polarized leaky lens antenna for wideband focal plane arrays," *IEEE Trans. on Antennas Propag.*, vol. 64, no. 8, pp. 3330–3337, Aug. 2016.

[25] S. O. Dabironezare, et al., "A dual-band focal plane array of kinetic inductance bolometers based on frequency-selective absorbers," *IEEE Trans. on Terahertz Sci. and Tech.*, vol. 8, no. 6, pp. 746–756, 2018.

[26] A. Nagamune and P. Pathak, "An efficient plane wave spectral analysis to predict the focal region fields of parabolic reflector antennas for small and wide angle scanning," *IEEE Trans. on Antenna and Propag.*, vol. 38, no. 11, pp. 1746–1756, Nov. 1990.

[27] S. O. Dabironezare, et al., "Coherent Fourier Optics model for the synthesis of large format lens based focal plane arrays," *IEEE Trans. on Antennas Propag., early access.*

[28] CST Microwave Studio. CST [Online] Available: http://www.cst.com/.

[29] S. O. Dabironezare, "Fourier Optics Field Representations for the Design of Wide Field-of-View Imagers at Sub-millimetre Wavelengths," PhD dissertation, Delft University of Technology, 2020, [Online]. Available: https://doi.org/10.4233/uuid:23c845e1-9546-4e86-ae77-e0f14272517b.

[30] D. Pasqualini and S. Maci, "High-frequency analysis of integrated dielectric lens antennas," *IEEE Trans. on Antennas Propag.*, vol. 52, no. 3, pp. 840–847, March 2004.

[31] S. O. Dabironezare, et al, "Quasi-Optical System for the ASTE Telescope with 1:3 Bandwidth at Sub-mm Wave," *44th International Conference on Infrared, Millimeter, and Terahertz Waves (IRMMW-THz)*, pp. 1-2, Paris, France, 2019.